Polymer 213 (2021) 123212

Contents lists available at ScienceDirect

Polymer

journal homepage: http://www.elsevier.com/locate/polymer

Synthesis of poly(styrene)-*b*-poly(2-vinyl pyridine) four-arm star block copolymers via ATRP and their self-assembly behaviors

Chia-Juei Hsu [a], Cheng-Wei Tu [b], Yu-Wen Huang [a], Shiao-Wei Kuo [c], Rong-Ho Lee [a], Yu-Ting Liu [d], Han-Yu Hsueh [e,**], Junko Aimi [f,***], Chih-Feng Huang [a,*]

[a] Department of Chemical Engineering, i-Center for Advanced Science and Technology (iCAST), National Chung Hsing University, Taichung, 40227, Taiwan
[b] Industrial Technology Research Institute, Chutung, Hsinchu, 31057, Taiwan
[c] Department of Materials and Optoelectronic Science, Center of Crystal Research, National Sun Yat-Sen University, Kaohsiung, 80424, Taiwan
[d] Department of Soil and Environmental Sciences, National Chung Hsing University, Taichung, 40227, Taiwan
[e] Department of Materials Science and Engineering, National Chung Hsing University, Taichung, 40227, Taiwan
[f] Research Center for Functional Materials, National Institute for Materials Science, 1-2-1 Sengen, Tsukuba, Ibaraki, 305-0047, Japan

ARTICLE INFO

Keywords:
Atom transfer radical polymerization
poly(styrene)
poly(2-vinyl pyridine)
Star block copolymers
Polymer self-assembly

ABSTRACT

In this study, synthesis of poly (styrene)-*b*-poly (2-vinyl pyridine) four-arm star block copolymers ((PS-*b*-P2VP)$_4$ sBCPs) possessing high interaction parameter (χ) feature was investigated. To obtain well-defined sBCPs, a challenge on ATRP of pyridine-containing monomers is foreseeable. We thus scrutinized the domino effect from PS macroinitiators (MIs) having different halogen chain ends (i.e., (PS–X)$_4$, where X = Br/Cl) to the subsequent chain extensions. As evident from the model reactions of benzyl halides (BzX, where X = Br/Cl) and 2-methylpyridine (2 MP), the combination of BzCl and 2 MP can significantly suppress the substitution side reaction. Consequently, well-defined (PS-*b*-P2VP)$_4$ sBCPs were obtained (M_n = ca. 58 k–82 k with PDI <1.5). From the analyses of small angle X-Ray scattering (SAXS), transmission electron microscopy (TEM), and atomic force microscope (AFM), self-assembly behaviors of the obtaining sBCPs were facilely observed due to the high χ feature, mainly including cylinder and lamellae morphologies, in nanoscale of approximately 30 nm.

1. Introduction

The evolutions of controlled/living radical polymerizations (CRPs) empower academic research and industrial outputs to afford well-defined (co)polymers with predictable molecular weights and low polydispersity (PDI). The evolved CRPs mostly comprise atom transfer radical polymerization (ATRP) [1–5], reversible addition-fragmentation chain transfer (RAFT) polymerization [6–10], and nitroxide-mediated radical polymerization (NMRP) [11,12]. Among them, a variety of ATRP techniques have been manifested their robustness to afford not only well-defined block copolymers (BCPs) but also various polymer architectures, such as star block copolymers (sBCPs) and miktoarm star copolymers (μ-*star*) [13–15].

BCPs with high interaction parameter (χ) features and/or star shapes are emerging research targets that can conduct fascinating self-assembly behaviors classifying as the "bottom-up" process. The self-assembly nanostructures generally exhibit ordered spheres (Sph), cylinders (Cyl), periodic gyroid (Gyr), and lamellae (Lam) types. Recently, an unprecedented analogue Frank-Kasper (F–K) microphase self-assembled from architectural symmetry/asymmetry soft matters with/without additives was disclosure [16,17]. The F–K microphase basically belongs to the low-symmetry sphere phases, such as A15 and σ phases. Therefore, the combinations of "bottom-up" process (i.e., BCP self-assembly) and "top-down" process (i.e., lithography) could support the evolutions of semiconductor process technology for the fabrications of electronics with sub-micron feature sizes. Several high-χ systems have been studied from the synthetic challenge to the microphase separation behaviors [18–21]. In addition, star-shaped copolymers possess the "entropy penalty" effect to effortlessly conduct the self-assembly process [22–27]. For examples, Russell and co-workers [28–31] demonstrated segmented copolymers comprising poly (styrene)/poly (2-vinyl pyridine) (PS/P2VP, where χ = 0.18), including AB diblock, ABA triblock,

* Corresponding author.
** Corresponding author.
*** Corresponding author.
E-mail addresses: hyhsueh@dragon.nchu.edu.tw (H.-Y. Hsueh), AIMI.Junko@nims.go.jp (J. Aimi), HuangCF@dragon.nchu.edu.tw (C.-F. Huang).

https://doi.org/10.1016/j.polymer.2020.123212
Received 31 August 2020; Received in revised form 31 October 2020; Accepted 6 November 2020
Available online 10 November 2020
0032-3861/

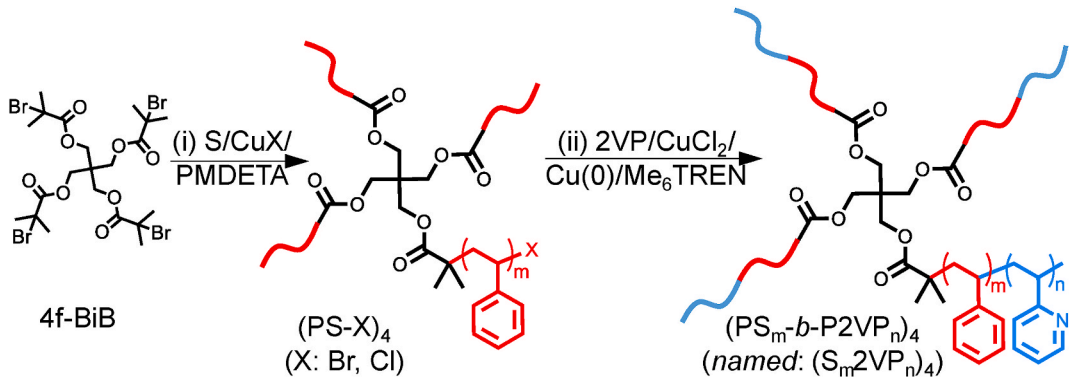

Scheme 1. Synthesis of PS-*b*-P2VP four-arm (sBCPs) [(i) normal ATRP: S/CuX/PMDETA = 1500/1/4/4 at 80 °C in anisole. (ii) AGET ATRP: 2VP/(PS–X)$_4$/$CuCl_2$/Cu(0)/Me_6TREN = 2000/1/1/3/8 at 80 °C].

A_2B/ABC μ-star, and three-/four-arm star block copolymers. They further demonstrated that different architectures of salt-doped multi--arm (PS-*b*-P2VP)$_n$ sBCPs enhanced the ordering of the sBCPs, enabling the generation of nanostructures with microdomain periods less than 10 nm. Hadziioannou et al. [32] studied the phase behaviors and association properties of a series of five miktoarm PS_nP2VP_m star copolymers (i.e., A_nB_m–typed μ-star). They found the *d*-spacing of lamellar structures of miktoarm star copolymers chain length (*N*) was diverged from the original $N^{2/3}$ law of diBCPs. Namely, self-assembly behaviors of PS-*b*-P2VP sBCPs are rarely disclosed, especially on the study of the morphologies of 4-arm (PS-*b*-P2VP)$_4$ sBCPs in the thin film states.

Thus we attempt to synthesize well-defined PS-*b*-P2VP sBCPs via ATRP technique which is still quite challenge. In another CRP example, Lowe and co-workers [33] studied RAFT polymerizations of 2- and 4-vinylpyridines (2VP and 4VP) with nice controls using cumyl dithiobenzoate (CDB) and further conducted chain extensions of 4VP/2VP to afford well-defined (P2VP-*b*-P4VP)s. However, high temperatures are needed to obtain well-controlled RAFT polymerizations of styrene using CDB [34] and the synthesis of multi-functional chain transfer agent (CTA) would be another challenge in practical concerns. In another example, Zhu group [35] investigated Cu(0)-mediated CRP of 2VP which assisted by specific solvent serving as strong hydrogen bonding donor (i.e., 1,1,1,3,3,3-hexafluoro-2-propanol (HFIP)) to form "2VP-HFIP supramonomer". The supramonomer structure redistributed the electron density of 2VP monomer and led to undergo well-controlled Cu(0)-mediated CRP. Nevertheless, we could expect a poor solubility of PS macroinitiators (MIs) in HFIP that would lead to uncontrolled fashion during chain extensions. Namely, the synthesis of PS-*b*-P2VP sBCPs via ATRP techniques is still limited.

Beneficial from ATRP systems, we can facilely attain multi-functional initiators. As shown in Scheme 1, a tetra-functional initiator (i.e., 4f-BiB) was synthesized. Similar initiating sites (i.e., alkyl 2-bromopropionate) to achieve well control of ATRP of styrene (S) were reported [2,36,37]. We thus carry out normal ATRP of S with 4f-BiB and different copper catalysts (I.e., CuBr and CuCl). We investigated the domino effect from the obtaining PS macroinitiators (MIs) having different chain ends (i.e., (PS–X)$_4$; X = Br or Cl) to the subsequent chain extensions. We thus scrutinized the challenges on chain extensions of (PS–X)$_4$ MIs with 2-vinyl pyridine (2VP) to attain well-defined (PS-*b*-P2VP)$_4$ sBCPs. The self-assembly behaviors of (PS-*b*-P2VP)$_4$ sBCPs in the solid-state were analyzed by small angle X-Ray scattering (SAXS), transmission electron microscopy (TEM), and atomic force microscope (AFM).

2. Experimental

2.1. Materials

Styrene (S), 2-vinyl pyridine (2VP), copper (I) bromide (CuBr, 98%), copper (I) chloride (CuCl, 97%), copper (II) chloride ($CuCl_2$, 99%), copper powder (Cu(0), 150 mesh, 99.5%), *N*,*N*,*N*′,*N*″,*N*″-pentamethyldiethylenetriamine (PMDETA, 99%), and alumina (neutral) were purchased from Sigma–Aldrich. Benzyl bromide (BzBr, 98%), benzyl chloride (BzCl, 97%), 2-methylpyridine (2 MP), and naphthalene were ordered from TCI. Syntheses of pentaerythritol tetrakis (2-bromoisobutyrate) (4f-BiB) and tris [2-(dimethylamino)ethyl]amine (Me_6TREN) were referred to previous literature [38,39]. The FT-IR and ^{1}H NMR spectra of 4f-BiB were shown in Fig. S1 (see the Supporting Information). Solvents and monomers were distilled prior to use.

2.2. Characterization

The monomer conversions were monitored by a Hewlett–Packard gas chromatograph (GC) set with a CD-5 column and an FID detector (HP 5890 ser. II). Bruker 400 NMR spectrometer was employed to record ^{1}H NMR spectra were recorded using $CDCl_3$ (7.26 ppm) for chemical shift (δ = ppm) calibration. A gel permeation chromatography (GPC) equipped with two PSS SDV columns in series (linear S and 100 Å) and a RI detector (Waters 410) was conducted at 40 °C (eluent: tetrahydrofuran (THF); flow rate: 1 mL/min). Characterization of average molecular weights (i.e., M_n and M_w) and polydispersity (PDI = M_w/M_n) was estimated from a polystyrene-based calibration line. FT-IR spectra were collected by PerkinElmer Spectrum One to discriminate the functional groups of the drop-casted samples on KBr disks. Bulk sBCP samples were first heated to 140 °C with a heating rate of 60 °C/min and kept isotherm for 15 min to eliminate their thermal histories. Thermally treated bulk samples were attained after rapidly cooling at a rate of 150 °C/min from the melt state. Differential scanning calorimetry (DSC) of Seiko 6220 was employed to detect the glass transition (T_g) of star block copolymers (sBCPs) in the 2nd run (from 50 to 180 °C with 20 °C/min ramping rate under nitrogen atmosphere). A thermogravimetric analysis (TGA) instrument of TA Q50 was applied to measure the thermal stability of the samples (from 30 to 700 °C under nitrogen with 20 °C/min ramping rate). Small-angle X-ray scatterings (SAXS) were measured at the Endstation BL23A1 beamline of the National Synchrotron Radiation Research Center (NSRRC), Taiwan. The energy of X-ray source and the sample-to-detector distance were 15 kV and 3 m, respectively. The *d*-spacing values were calculated from the first scattering peaks (q^*) using the formula of $d = 2\pi/q^*$. Bright-field transmission electron microscope (TEM) images were obtained using the mass-thickness contrast with a JEOL JEM-2010 LaB6 at an accelerating voltage of 200 kV. Topological images were measured at room temperature by using Dimension-3100 atomic force microscope (AFM) with an Olympus AC200TS microcantilever. The sBCPs solutions (3 wt% in THF) were spin-coated on a Si wafer with a SiO_2 surface (3000 rpm, 1 min) and sBCP thin films with thicknesses of 150–300 nm were attained.

Table 1
Chain extensions of $(PS–X)_4$ MIs with 2VP and characterization.

Entry[a] (#)	MI	Conv. (%)	$M_{n,GPC}$[b]	PDI[b]	$M_{n,NMR}$[c]	Simple abbr.
1	$(PS_{89}–Br)_4$	15	37,020	2.33	54,640	$(S_{89}2VP_{42})_4$
2	$(PS_{89}–Cl)_4$	14	37,230	1.18	64,440	$(S_{89}2VP_{65})_4$
3	$(PS_{89}–Cl)_4$	25	39,230	1.39	81,520	$(S_{89}2VP_{105})_4$
4	$(PS_{100}–Cl)_4$	10	40,070	1.24	58,500	$(S_{100}2VP_{41})_4$
5	$(PS_{100}–Cl)_4$	16	41,870	1.49	66,800	$(S_{100}2VP_{60})_4$

[a] 2VP/MI/$CuCl_2$/Cu(0)/Me_6TREN = 2000/1/1/3/8 at 80 °C; $[2VP]_0$ = 9.4 M.
[b] Values of M_n and PDI were measured by GPC (eluent: THF), with polystyrene standards for calibration. Repeating units of S_m can be obtained.
[c] The molar ratios of PS and P2VP were estimated by m: n = $[(A_{6.2–7.25ppm} - 3 \times A_{8.1–8.5ppm})/5H]$: $[A_{8.1–8.5ppm}/1H]$. By combining with the pre-determined m values from the GPC measurements, the repeating units of P2VP can be estimated (i.e., $2VP_n$).

2.3. Model reactions

An example: A Schlenk flask was charged with BzBr (0.19 mL, 1.62 mmol), 2 MP (2.0 mL, 20.3 mmol), acetone (3.6 mL), and small amounts of naphthalene (i.e., internal standard). An initial sample was taken. The reaction flask was sealed and carried out the reaction at ambient. The conversions of the model reactions were analyzed by ^{1}H NMR according to the consumption of BzBr or BzCl reactant.

2.4. Synthesis of four-arm star $(PS–X)_4$ by normal ATRP

A general procedure [40]: A Schlenk flask was charged with 4f-BiB (95 mg, 0.13 mmol), PMDETA (0.1 mL, 0.52 mmol), S (15 mL, 130 mmol). The bottle was sealed and degassed through few freeze/-pump/thaw cycles. In a frozen state, CuCl (51 mg, 0.52 mmol) was added and additionally degassed through two freeze–pump–thaw cycles (S/4f-BiB/CuCl/PMDETA = 1000/1/4/4; $[S]_0$ = 8.7 M). Prior to conducting reaction, t_0 reference was taken using anisole as the internal standard and the solution was immersed in an oil bath with 80 °C. The conversion of the monomer and the molecular weight (MW) of the polymer were analyzed by using GC and GPC, respectively. The reaction was ended with a conversion of less than 40% by placing the flask into an ice bath, exposed to air, and diluted by THF. The mixture was filtered by alumina and precipitated in methanol. The resulting white powder of $(PS–Cl)_4$ macroinitiator (MI) can be collected ($M_{n,GPC}$ = 41,870 and PDI = 1.16). The dried samples were stored in a dry box.

2.5. Chain extensions of $(PS–X)_4$ with 2VP via AGET ATRP

A typical procedure [41]: solids of $(PS–Cl)_4$ MI (0.63 g, 0.015 mmol), $CuCl_2$ (2 mg, 0.015 mmol), and Cu powder (3 mg, 0.045 mmol) were added to a Schlenk flask. The flask was degassed and backfilled with nitrogen gas. Then degassed 2VP (3.2 mL, 30 mmol) and Me_6TREN (42 μL, 0.20 mmol) were added into the flask (2VP/$(PS–Cl)_4$/$CuCl_2$/Cu (0)/Me_6TREN = 2000/1/1/3/8; $[2VP]_0$ = 9.4 M). The flask was sealed and placed in a thermostatted bath at 80 °C. Conversions of the reaction were periodically monitored by GC using anisole as the internal standard. The purification steps were similar to the above-mentioned but precipitated in hexane. The light-brownish solid was collected and dried overnight to obtain (PS-*b*-P2VP)$_4$ star block copolymer (sBCP) ($M_{n,NMR}$ = 65,950; $M_{n,GPC}$ = 37,230 and PDI = 1.18). Due to the hydrodynamic differences, the $M_{n,NMR}$ value was utilized to identify the sBCP information. The chain extension results were summarized in Table 1. For the latter physical properties discussion (i.e., after Fig. 7), we herein named sBCP as $(S_n2VP_m)_4$. The m and n values inside the bracket represent the degree of polymerization and the value outside the bracket is arm numbers. Densities of PS with d_{PS} = 1.06 and P2VP with d_{P2VP} = 1.15 were utilized to estimate volume fractions (Φ) of each block in the $(S_n2VP_m)_4$ sBCP.

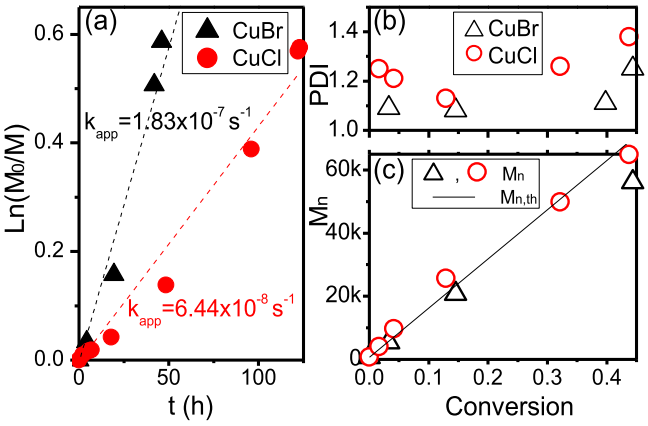

Fig. 1. (a) ATRP first-order kinetic plot and (b, c) M_n/PDI vs conversion plots (S/4f-BiB/CuX/PMDETA = 1000/1/4/4 at 80 °C; X = Br or Cl; $[S]_0$ = 8.7 M).

3. Results and discussion

Fig. 1 shows the kinetic plots of normal ATRP of styrene (S) at 80 °C (S/4f-BiB/CuX/PMDETA = 1000/1/4/4; X = Br or Cl $[S]_0$ = 8.7 M). Using CuBr as the catalyst (i.e., curve a in Fig. 1a: $k_{app,\ CuBr} = 1.83 \times 10^{-7}\ s^{-1}$), a linear first-order reaction and moderate reaction rate were obtained. Using CuCl as the catalyst (i.e., curve b in Fig. 1a: $k_{app,\ CuCl} = 6.44 \times 10^{-8}\ s^{-1}$), a linear first-order reaction was also obtained but we observed a slower reaction rate (ca. 2.8 times); than that of using CuBr. With the same initiating side from 4f-BiB, the activation rate constants (k_{act}) of using CuCl should be similar to that of using CuBr. With the polymerization proceedings, a notable difference of k_{app}s in Fig. 1a was acquired. Since k_{act} depends on the types of initiating sites, the original α-bromoisobutyrate sites will be exchanged to α-chloroisobutyrate when CuCl was used [8,10]. The k_{act} of chloride chain ends are lower than of bromide chain ends, resulting in a lower $k_{app,\ CuCl}$ value compared to that of $k_{app,\ CuBr}$. Therefore, the halogen exchange reactions led to a slower polymerization rate. As shown in Fig. 1c and b, we both acquired linear growth of molecular weights (MWs) up to M_n = ca. 60 k with narrow molecular weight distributions (i.e., PDI < 1.4). Fig. 2 displayed the corresponding GPC traces in Fig. 1. MW evolutions with mono-modal distribution were attained in a conversion of less than 40%. With higher conversions (i.e., >40%), a small peak of higher MW was observed in Fig. 2a and slightly broad distribution was obtained in Fig. 2b, which might be resulted from star-star coupling reactions [39]. Thus, controlled/living polymerization fashions and well-defined $(PS–X)_4$ four-arm star homopolymers (X = Br or Cl) can be obtained with moderate conversions (i.e., <40%).

Concerning about the chain ends, the obtaining two types of $(PS–X)_4$ macroinitiators (MIs) belong to a similar analogue of ATRP initiator of benzyl halides. The next step is to conduct chain extensions of MIs with 2-vinyl pyridine (2VP). However, it has been reported that pyridine groups can facilely react with alkyl/benzyl halides to form pyridinium salts through nucleophilic substitution reactions which could play as an interference to achieve well-controlled chain extensions [42]. Prior to the subsequent polymerizations, our attempt is thus to carry out model reactions of benzyl halides (i.e., BzX, where X = Br or Cl) and 2-methyl pyridine (2 MP). The reactions and the resulting ^{1}H NMR traces with various reaction times were displayed in Fig. 3 (BzX/2 MP = 1/12.5 in acetone at ambient). Conversions of the limited compounds can be estimated from the related ratios of a reference peak of naphthalene internal standard (δ = ca. 7.7 ppm) and the peak a (δ = ca. 5.45 ppm) of BzX. One new peak a' (δ = ca. 6.18 ppm) resulted from the pyridinium product can be acquired. In the case of BzBr/2 MP (i.e., Fig. 3B and C), we can slightly observe a small amount of pyridinium product from the initial timing (t_0) and acquire a high conversion (ca. 83%) of BzBr in 3 h, illustrating a fast substitution reaction between BzBr and 2 MP. In the

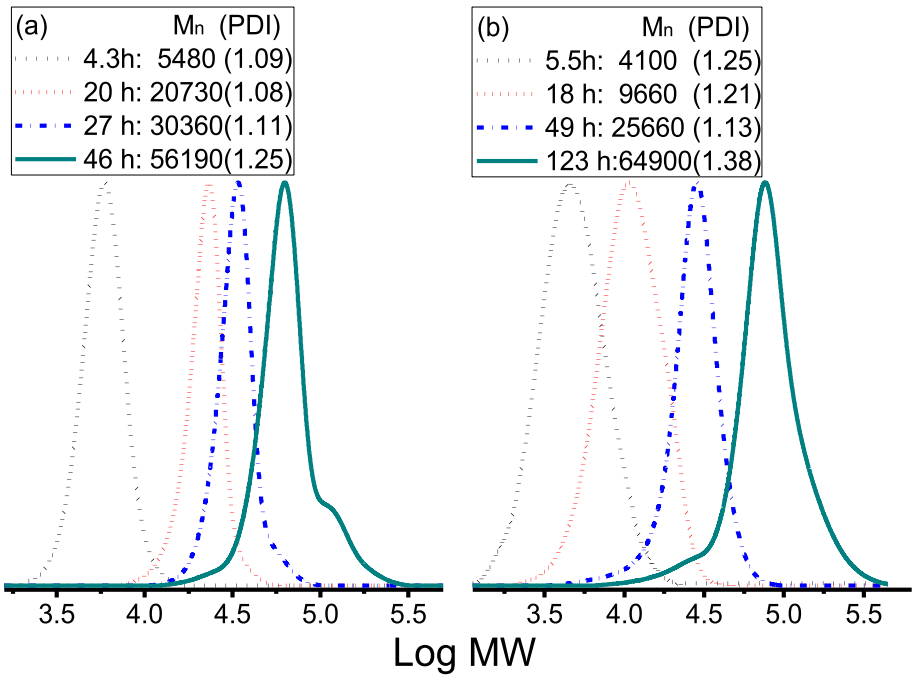

Fig. 2. GPC traces of the corresponding ATRPs of S in Fig. 1 with catalysts of (a) CuBr and (b) CuCl.

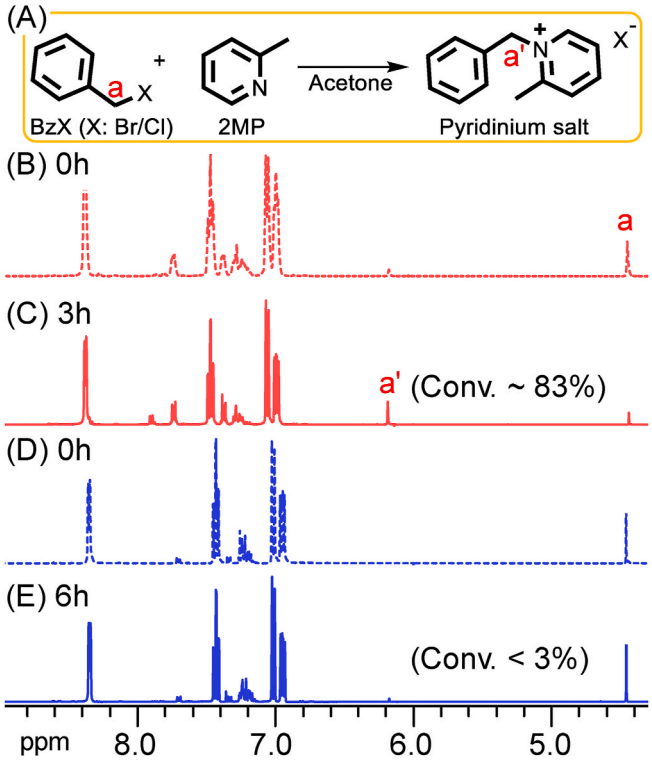

Fig. 3. (A) Model reaction scheme. Results of ^{1}H NMR spectra from (B, C) BzBr/2 MP and (D, E) BzCl/2 MP with various reaction times (BzX/2 MP = 1/12.5 in acetone at ambient with naphthalene as the internal standard).

case of BzCl/2 MP (i.e., Fig. 3D and E), we observed a much slower reaction compared to the former case and a low conversion (<3%) of BzCl was acquired. Revealing from these results, our subsequent chain extensions of 2VP might encounter fast substitution reactions between benzylic bromide and 2-substituted pyridines and vary the chain end functionality, leading to the formation of branching structures.

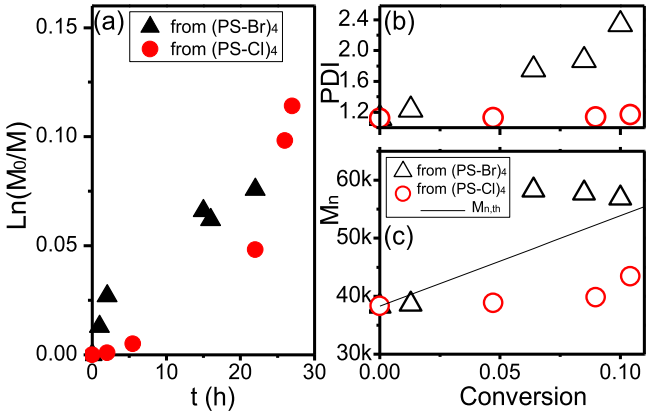

Fig. 4. Chain extensions of $(PS–X)_4$ MIs with 2VP: (a) first-order kinetic plot and (b, c) M_n/PDI vs conversion plots (2VP/MI/$CuCl_2$/Cu(0)/Me_6TREN = 2000/1/1/3/8 at 80 °C; $[2VP]_0$ = 9.4 M).

Alternatively, combinations of benzylic chloride and 2-substituted pyridines might efficiently suppress side reactions and lead to good control.

Subsequently, we conduct chain extensions of $(PS–X)_4$ MIs with 2VP via AGET ATRP (i.e., step (ii) in Scheme 1: 2VP/$(PS–X)_4$/$CuCl_2$/Cu(0)/Me_6TREN = 2000/1/1/3/8 at 80 °C; $[2VP]_0$ = 9.4 M). Notably, using a strong ligand, such as Me_6TREN, is necessary to suppress the competitions of copper chelating from 2VP [42]. In addition, AGET ATRP technique can elude freeze–pump–thaw cycles that might obtain a heterogeneous mixture due to poor solubility of MIs in the solution during recovery from the frozen state. Also, the copper complexes deactivated by the small amounts of oxygen in the solution can be also regenerated [41,43]. Kinetic plots of the chain extensions of MIs with 2VP were displayed in Fig. 4. In the case of $(PS–Br)_4$ (i.e., triangle symbols in Fig. 4), a gradual consumption of 2VP in the early stage but nearly pause in the latter stage was observed. A fast consumption from the $(PS–Br)_4$ MI was due to a fast activation rate constant of benzylic bromide initiating sites at the chain ends. As shown in Fig. 4b and c, however, the corresponding PDI values increased promptly (>1.7) and the MWs did

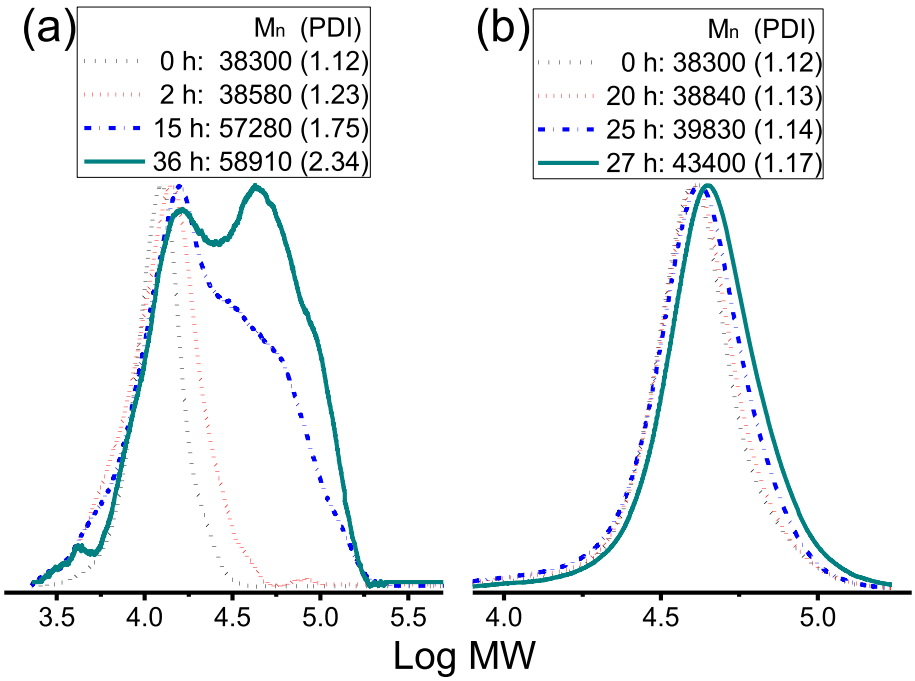

Fig. 5. GPC traces of the corresponding chain extensions of (a) $(PS–Br)_4$ and (b) $(PS–Cl)_4$ MIs with 2VP in Fig. 4.

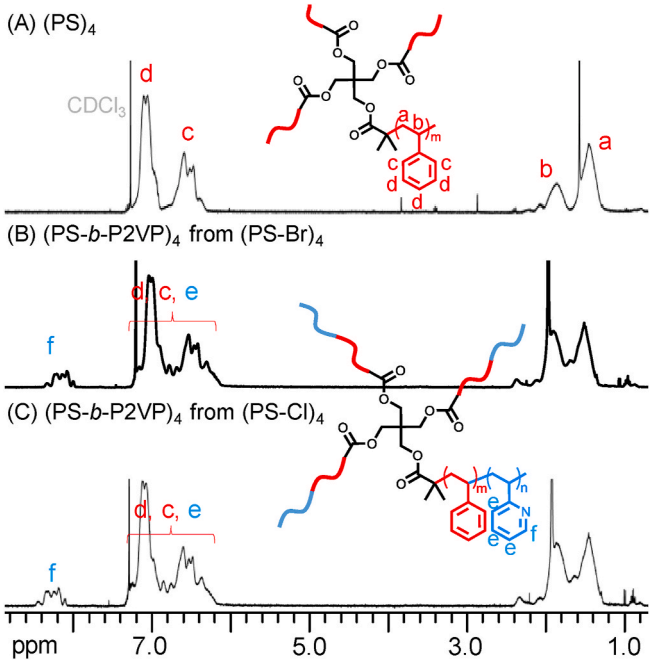

Fig. 6. ^1H NMR (400 MHz, $CDCl_3$) spectra of four-arm star (co)polymers: (A) $(PS)_4$, (B) $(PS\text{-}b\text{-}P2VP)_4$ extended from $(PS–Br)_4$, and (C) $(PS\text{-}b\text{-}P2VP)_4$ extended from $(PS–Cl)_4$.

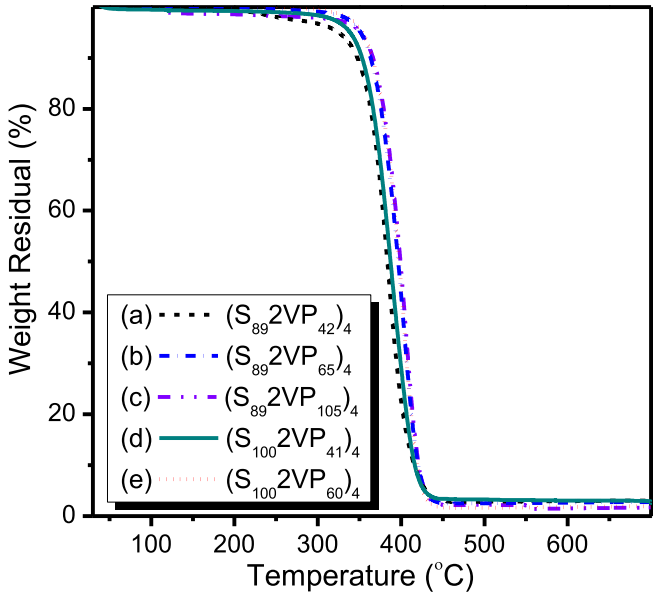

Fig. 7. TGA thermograms of PS-*b*-P2VP sBCPs under nitrogen (range: 30–700 °C; ramping: 20 °C/min).

not show significant increases. From the corresponding GPC traces in Fig. 5a, bi-modal distributions of GPC traces were observed, indicating significant side reactions have occurred during the chain extension of $(PS–Br)_4$ with 2VP, such as the aforementioned substitution reactions or coupling reactions [44,45]. In the case of $(PS–Cl)_4$ (i.e., circle symbols in Fig. 4), an induction period in the early stage and gradual consumptions of 2VP in the latter stage were acquired. As correspondingly shown in Fig. 4b, low PDI values (<1.2) were attained. As shown in Fig. 4c, we could correspondingly observe gradual increases of the MWs. The MW biases were due to the hydrodynamic difference between the obtaining $(PS\text{-}b\text{-}P2VP)_4$ four-arm star block copolymers (sBCPs) and the linear polystyrene calibration standards. From the corresponding GPC traces in Fig. 5b, mono-modal distributions of GPC traces were observed, indicating a good control fashion.

In Fig. 6, ^1H NMR (400 MHz, $CDCl_3$) spectra of the obtaining (co) polymers were demonstrated. Typical PS signals were shown in Fig. 6A spectrum, including peaks a–d. Fig. 6B and C displayed (PS-*b*-P2VP) star copolymers through chain extension from $(PS–Br)_4$ and $(PS–Cl)_4$ MIs, respectively. Comparing the spectra, notable P2VP signals were both observed (i.e., peaks e and f), indicating insignificantly chemical structure variations of the copolymers with bi-modal and mono-modal distributions. Based on M_n of the first PS block and estimated from the area

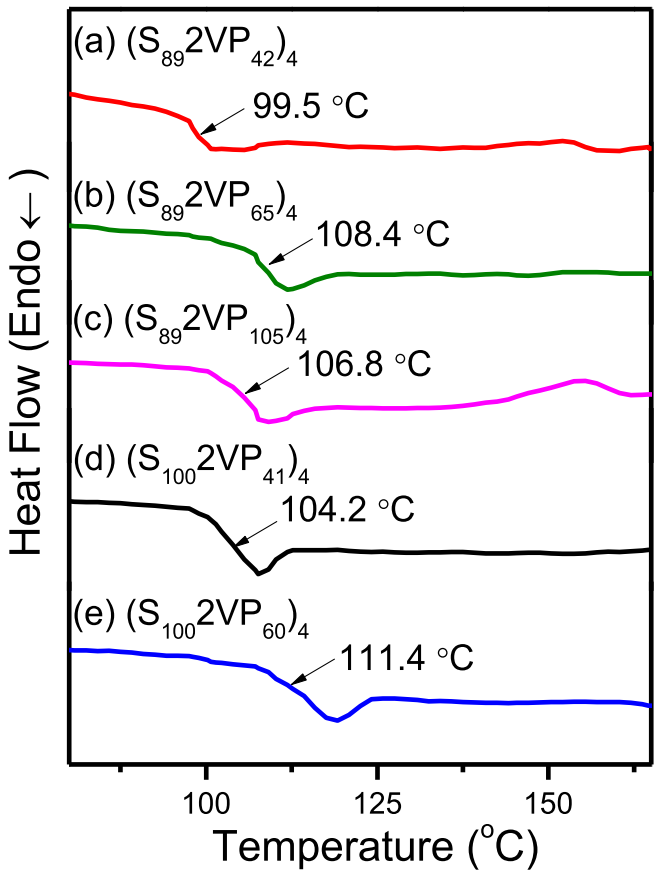

Fig. 8. DSC traces of $(S_m2VP_n)_4$ sBCPs under nitrogen (range: 50–180 °C; ramping: 20 °C/min).

ratio of f (ca. 7.25 ppm) and c–e (ca. 6.1–7.25 ppm), we can obtain the m and n repeating units in each block (i.e., obtaining $(PS_m$-*b*-$P2VP_n)_4$ sBCPs). Fig. S2 shows the corresponding FT-IR spectra of the samples in Fig. 6. The chain extension conditions and characterization were summarized in Table 1. Using simple abbreviations for the latter discussion, notably, we further named the obtaining sBCPs in the form of $(S_m2VP_n)_4$ as illustrated in Table 1.

We then measure the thermal stability of the sBCPs by using thermogravimetric analysis (TGA) under a constant nitrogen flow. As shown in Fig. 7, the obtaining $(S_m2VP_n)_4$ samples performed similar TGA profiles with single-step pyrolysis. The maximum decomposition rates (r_ds) of the sBCP were all at ca. 400 °C. The temperatures of five weight percent loss ($T_{d5\%}$) and char yield were around 320 °C and 3 wt%, respectively. In Fig. 8, differential scanning calorimetry (DSC) traces of the $(S_m2VP_n)_4$ sBCPs were displayed. In $(S_{89}2VP_{42})_4$ sBCP, single T_g with a value of 99 °C was acquired that might be due to its broad molecular weight distribution (i.e., PDI = 2.33). In other cases of $(S_m2VP_n)_4$ sBCPs, single T_gs in a range of 104–111 °C were observed. Table 2 listed the characterization of the TGA and DSC properties. Basically, the miscibility of different polymeric segments can be preliminarily analyzed by using DSC. In our case, however, pure PS and P2VP homopolymers have similar T_g values at around 105 °C which was thus difficult to discriminate the miscibility between PS and P2VP segments on the basis of DSC traces.

Next, we attempt to study the formation of well-ordered nanostructures from the self-assembly of $(S_m2VP_n)_4$ sBCPs in the bulk state. The samples were thermally treated to eliminate their thermal histories before one-dimensional SAXS and TEM identification. As mentioned above, the T_gs of the $(S_m2VP_n)_4$ sBCPs based on the DSC measurements in Fig. 8 were in a range of 100–111 °C. For $(S_{89}2VP_{42})_4$ (Φ_{PS} = 70%), the SAXS result (Fig. 9a) shows a blurred scattering profile without definite reflection peaks, indicating a disordered structure. The microphase separation structures can be further examined in TEM images after ruthenium tetroxide (RuO_4) staining as shown in Fig. 10a. Notably, the RuO_4 complexed with the double bonds in the PS blocks, rendering the PS microdomains in dark regions due to the mass-thickness contrast. By contrast, the bright regions can be referred to the P2VP microdomains under TEM observation. Similar to the SAXS results, the corresponding TEM image further reveals dark spherical domains dispersed in a bright matrix without definite self-assembled morphologies. The observed disordering of self-assembled nanostructures should be attributed to the large PDI value of the $(S_{89}2VP_{42})_4$ (i.e., PDI = 2.33, Table 1), leading to insufficient self-assembly tendency.

We then examined the other sBCP samples with small PDI values (i.e., PDI < 1.5, Table 1). In the $(S_{89}2VP_{65})_4$ (Φ_{PS} = 60%) sample, we acquired a well-ordered cylindrical phase with hexagonal packing reflected in the 1D SAXS profile (i.e., Fig. 9b) with the *q* ratios of 1: $\sqrt{3}$: $\sqrt{4}$: $\sqrt{7}$. Using the primary peak, the *d*-spacing of the (100) plane was determined as 34.4 nm and the interspacing of each cylinder was then calculated as 39.8 nm. Bright cylinder-forming domains of the P2VP part were well-dispersed in a dark matrix of the PS part as shown in TEM images (i.e., Fig. 10b). In the $(S_{89}2VP_{105})_4$ (Φ_{PS} = 48%) sample, the self-assembled morphology was identified as a lamellar phase according to the reflection peaks at the *q* ratios of 1: 2: 3 shown in Fig. 9c. The *d*-spacing of the (100) plane was determined as 33.2 nm from the primary peak of the reflections. The corresponding TEM image (i.e., Fig. 10c) showed alternative dark and bright sheets, confirming the lamellar nanostructure of the $(S_{89}2VP_{105})_4$ (Φ_{PS} = 0.48) from the self-assembly in the melt state. In the samples of $(S_{100}2VP_{41})_4$ (Φ_{PS} = 0.72) and $(S_{100}2VP_{60})_4$ (Φ_{PS} = 0.64), because of the larger PS volume fractions, well-ordered cylindrical phases were both observed. Fig. 9d and e demonstrated the corresponding 1D SAXS profiles while Fig. 10d and e represented the corresponding TEM images. Notably, obvious black and bright sheets can be observed as shown in Fig. 10c (such as the point of the white arrow). Nano-sheet structures are critical features of lamellar phase from polymer self-assembly. TEM image of $(S_{89}2VP_{105})_4$ (Φ_{PS} = 0.48) sample was thus identified as a lamellar nanostructure. We also examined the spin-coating films of the sBCPs to analyze their self-assembly behaviors. As shown in Fig. 10a'–10e', the tapping mode

Table 2
Characteristics of thermal properties and morphology of the 4-arm sBCPs.

Sample	$T_{d5\%}$[a] (°C)	Char yield (%)	T_g (°C)	Φ_{PS}[b]	SAXS results		TEM results		AFM results
					Morph.[c]	Size (nm)	Morph.[c]	Size (nm)	Morph.[c]
$(S_{89}2VP_{42})_4$	341.1	1.83	99.5	0.7	Dis	–	Dis-Sph	17.2	Dis-Sph
$(S_{89}2VP_{65})_4$	356.5	1.27	108.4	0.6	Cyl	34.4	Cyl	29.4	Cyl
$(S_{89}2VP_{105})_4$	344.4	1.29	106.9	0.48	Lam	33.2	Lam	32.5	2VP-Wet
$(S_{100}2VP_{41})_4$	365.4	1.34	104.2	0.64	Cyl	35.4	Cyl	31.1	Cyl
$(S_{100}2VP_{60})_4$	357.7	0.87	111.4	0.72	Cyl	33.4	Cyl	36.3	Cyl

[a] The temperatures at five weight percent loss of the $(S_m2VP_n)_4$ sBCPs.
[b] Φ_{PS}: volume fraction of the PS part.
[c] Dis: disorder; Cyl: cylinder; Lam: lamellae; Dis-Sph: disorder sphere; 2VP-Wet: P2VP preferential wetting via air.

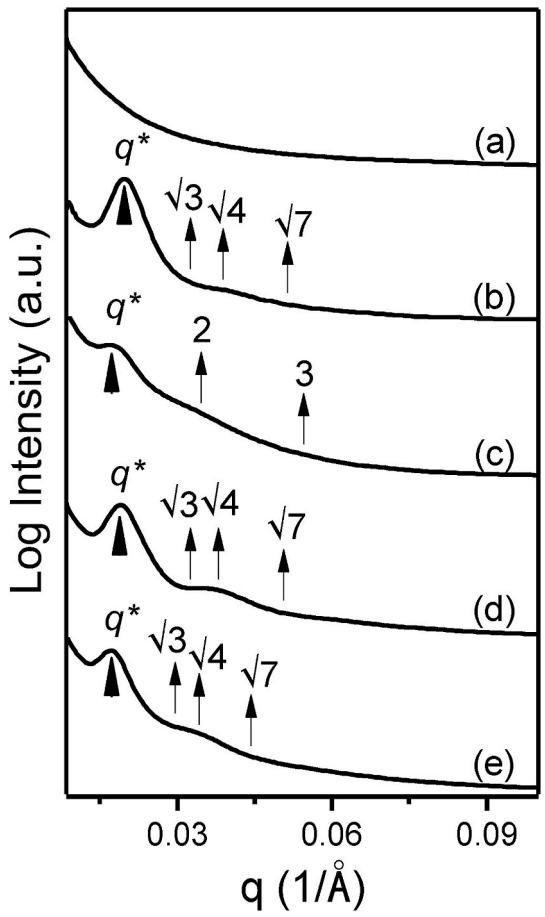

Fig. 9. SAXS profiles of (a) $(S_{89}2VP_{42})_4$ (Φ_{PS} = 0.7), (b) $(S_{89}2VP_{65})_4$ (Φ_{PS} = 0.60), (c) $(S_{89}2VP_{105})_4$ (Φ_{PS} = 0.48), (d) $(S_{100}2VP_{41})_4$ (Φ_{PS} = 0.72), and (e) $(S_{100}2VP_{60})_4$ (Φ_{PS} = 0.64) (Φ_{PS}: volume fraction of the PS part).

atomic force microscopy (AFM) phase images clearly displayed the corresponding nanostructures. Notably, the darker areas in the phase image are attributed to the stiff PS domains and the brighter areas belong to the soft P2VP domains. We thus attained disorder (i.e., Fig. 10a') and cylinders (i.e., Fig. 10b', 10d', and 10e') morphologies. In the sample of $(S_{89}2VP_{105})_4$ thin films (Fig. 10c'), distinctively, we observed minor dark PS domains dispersed in the brighter P2VP wetting matrix. It is plausibly the affinity effect by which air exhibits preferential selectivity toward the P2VP blocks, resulting in the formation of a P2VP wetting layer. The characterization of sBCPs from SAXS, TEM, and AFM were summarized in Table 2.

It has reported the phase diagram of PS-*b*-P2VP diBCP [46]. As displayed in Fig. S3 (see the Supporting Information), the microphase separation morphologies of linear and star BCPs are similar. Cyl morphology exists at PS volume fractions f_{PS}) from 0.60 to 0.75 [i.e., $(S_{89}2VP_{65})_4$, $(S_{89}2VP_{65})_4$, and $(S_{100}2VP_{60})_4$] and Lam morphology is presented at f_{PS}) around 0.50 [i.e., $(S_{89}2VP_{105})_4$]. By comparing further details, however, the Cyl morphology has a slightly broader region in the case of the 4-arm sBCPs. The difference might be attributed to the less symmetricity and more congested center of the sBCP chains. These lead to forming curve interfaces of PS and P2VP polymer chains which are briefly illustrated in the inserted figures. Thus cylindrical structures could be easily generated during self-assembly process. Note that controlling thin film morphologies is quite a challenge that might be sensitive to the molecular weight, surface energy of constituted components, interactions among copolymers and substrate/air, polymer topology, and thickness of the thin film samples. Hence, systematic studies on the phase behaviors of sBCP thin films, such as the order-disorder and order-order transition boundaries, are currently in progress.

4. Conclusions

We synthesized well-defined $(PS–X)_4$ MIs (PDI < 1.4) with various chain ends (X = Br or Cl) via normal ATRP. Then a significant substitution side reaction was revealed from the model reactions of BzX and 2 MP, illustrating the importance of the chain end to suppress the subsequent chain extensions of $(PS–X)_4$ MIs with 2VP. A s a result, well-defined four-arm $(PS\text{-}b\text{-}P2VP)_4$ sBCPs (M_n = ca. 58 k–82 k with PDI <1.5) can be synthesized by using AGET ATRP in proper conditions. From the analyses of SAXS, TEM, and AFM, self-assembly behaviors of the obtaining sBCPs driven from the highly incompatible of the P2VP and PS blocks were facilely revealed. Nanostructures, mainly including cylinder and lamellae morphologies, in a scale of approximately 30 nm were attained.

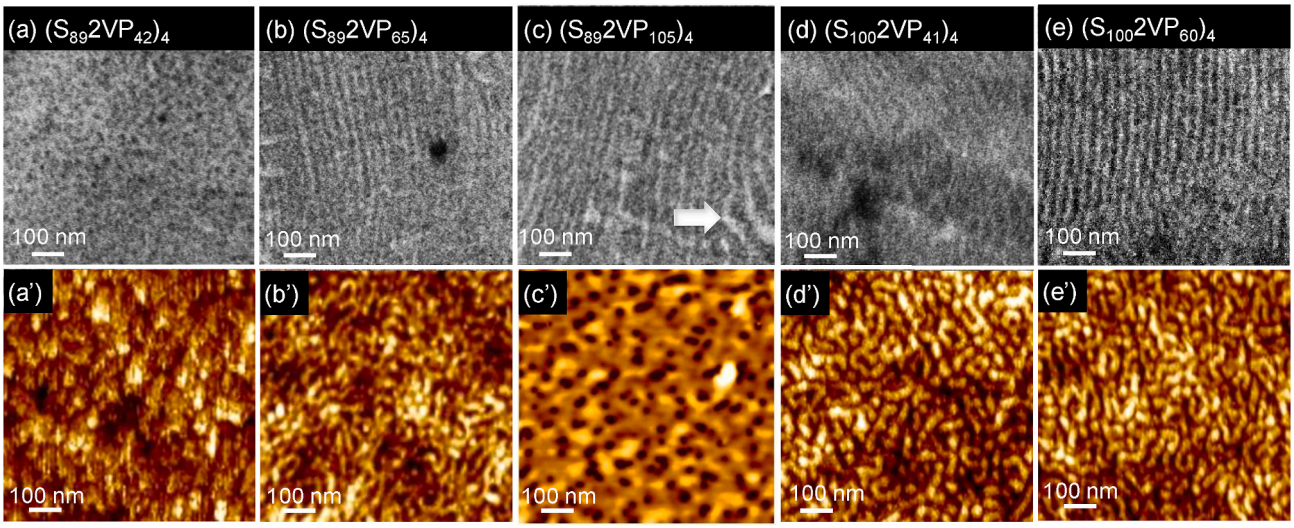

Fig. 10. TEM micrographs of (a) $(S_{89}2VP_{42})_4$, (b) $(S_{89}2VP_{65})_4$, (c) $(S_{89}2VP_{105})_4$, (d) $(S_{100}2VP_{41})_4$, and (e) $(S_{100}2VP_{60})_4$ sBCPs (note: dark areas from PS domains while bright areas from P2VP domains). (a')–(e') Tapping-mode AFM phase images of the corresponding sBCPs (note: darker areas relating to PS domains and brighter areas relating to P2VP domains based on the chain stiffness).

Declaration of competing interest

The authors declare that they have no known competing financial interests or personal relationships that could have appeared to influence the work reported in this paper.

Acknowledgements

The authors acknowledge the financial support from the Ministry of Science and Technology (MOST109-2221-E-005-071 and MOST108-2923-E-005-001-MY2), NCHU ENABLE Center Project (no.: 109ST001G), TCVGH-NCHU Joint Research Program (no.: 1097605-109S0703A), and TCUS Exchange Project. SAXS experiments assisted in the National Synchrotron Radiation Research Center ((NSRRC), Taiwan) were deeply acknowledged.

Appendix A. Supplementary data

Supplementary data to this article can be found online at https://doi.org/10.1016/j.polymer.2020.123212.

References

[1] J.S. Wang, K. Matyjaszewski, Controlled living radical polymerization - atom-transfer radical polymerization in the presence of transition-metal complexes, J. Am. Chem. Soc. 117 (1995) 5614–5615.
[2] W. Tang, Y. Kwak, W. Braunecker, N.V. Tsarevsky, M.L. Coote, K. Matyjaszewski, Understanding atom transfer radical polymerization: effect of ligand and initiator structures on the equilibrium constants, J. Am. Chem. Soc. 130 (2008) 10702–10713.
[3] C.-F. Huang, S.-W. Kuo, H.-F. Lee, F.-C. Chang, A new strategy for the one-step synthesis of block copolymers through simultaneous free radical and ring opening polymerizations using a dual-functional initiator, Polymer 46 (2005) 1561–1565.
[4] Y.-S. Huang, H.-Y. Hsueh, J. Aimi, L.-C. Chou, Y.-C. Lu, S.-W. Kuo, C.-C. Wang, K.-Y. Chen, C.-F. Huang, Effects of various Cu(0), Fe(0), and proanthocyanidin reducing agents on Fe(III)-catalysed ATRP for the synthesis of PMMA block copolymers and their self-assembly behaviours, Polym. Chem. 11 (2020) 5147.
[5] A. Juhari, J. Mosnacek, J.A. Yoon, A. Nese, K. Koynov, T. Kowalewski, K. Matyjaszewski, Star-like poly(n-butyl acrylate)-*b*-poly(alpha-methylene-gamma-butyrolactone) block copolymers for high temperature thermoplastic elastomers applications, Polymer 51 (2010) 4806–4813.
[6] G. Moad, Y.K. Chong, A. Postma, E. Rizzardo, S.H. Thang, Advances in RAFT polymerization: the synthesis of polymers with defined end-groups, Polymer 46 (2005) 8458–8468.
[7] G. Moad, E. Rizzardo, S.H. Thang, Living radical polymerization by the RAFT process, Aust. J. Chem. 58 (2005) 379–410.
[8] C.-F. Huang, R. Nicolay, Y. Kwak, F.-C. Chang, K. Matyjaszewski, Homopolymerization and block copolymerization of *N*-vinylpyrrolidone by ATRP and RAFT with haloxanthate inifers, Macromolecules 42 (2009) 8198–8210.
[9] S. Perrier, P. Takolpuckdee, Macromolecular design via reversible addition-fragmentation chain transfer (RAFT)/Xanthates (MADIX) polymerization, J. Polym. Sci., Part A: Polym. Chem. 43 (2005) 5347–5393.
[10] C.-F. Huang, Y.-A. Hsieh, S.-C. Hsu, K. Matyjaszewski, Synthesis of poly(*N*-vinyl carbazole)-based block copolymers by sequential polymerizations of RAFT-ATRP, Polymer 55 (2014) 6051–6057.
[11] D. Benoit, V. Chaplinski, R. Braslau, C.J. Hawker, Development of a universal alkoxyamine for "living" free radical polymerizations, J. Am. Chem. Soc. 121 (1999) 3904–3920.
[12] C.J. Hawker, A.W. Bosman, E. Harth, New polymer synthesis by nitroxide mediated living radical polymerizations, Chem. Rev. 101 (2001) 3661–3688.
[13] C.-F. Huang, S.-W. Kuo, H.-C. Lin, J.-K. Chen, Y.-K. Chen, H. Xu, F.-C. Chang, Thermal properties, miscibility and specific interactions in comparison of linear and star poly(methyl methacrylate) blend with phenolic, Polymer 45 (2004) 5913–5921.
[14] C.F. Huang, Y.S. Huang, K.Y. Lai, Synthesis and self-assembly of Poly(*N*-octyl benzamide)-μ-poly(ε-caprolactone) miktoarm star copolymers displaying uniform nanofibril morphology, Polymer 178 (2019) 121582.
[15] C.F. Huang, J. Aimi, K.Y. Lai, Synthesis of novel mu-star copolymers with poly(*N*-octyl benzamide) and poly(epsilon-caprolactone) miktoarms through chain-growth condensation polymerization, styrenics-assisted atom transfer radical coupling, and ring-opening polymerization, Macromol. Rapid Commun. 38 (2017) 1600607.
[16] Z.B. Su, C.H. Hsu, Z.H. Gong, X.Y. Feng, J.B. Huang, R.M. Zhang, Y. Wang, J. L. Mao, C. Wesdemiotis, T. Li, S. Seifert, W. Zhang, T. Aida, M.J. Huang, S.Z. D. Cheng, Identification of a Frank-Kasper Z phase from shape amphiphile self-assembly, Nat. Chem. 11 (2019) 899–905.
[17] M.W. Bates, J. Lequieu, S.M. Barbon, R.M. Lewis, K.T. Delaney, A. Anastasaki, C. J. Hawker, G.H. Fredrickson, C.M. Bates, Stability of the A15 phase in diblock copolymer melts, Prod. Natl. Acad. Sci. U.S.A. 116 (2019) 13194–13199.
[18] M.J. Maher, C.M. Bates, G. Blachut, S. Sirard, J.L. Self, M.C. Carlson, L.M. Dean, J. D. Cushen, W.J. Durand, C.O. Hayes, C.J. Ellison, C.G. Willson, Interfacial design for block copolymer thin films, Chem. Mater. 26 (2014) 1471–1479.
[19] Y.D. Luo, D. Montarnal, S. Kirn, W.C. Shi, K.P. Barteau, C.W. Pester, P.D. Hustad, M.D. Christianson, G.H. Fredrickson, E.J. Kramer, C.J. Hawker, Poly (dimethylsiloxane-*b*-methyl methacrylate): a promising candidate for sub-10 nm patterning, Macromolecules 48 (2015) 3422–3430.
[20] D.P. Sweat, M. Kim, S.R. Larson, J.W. Choi, Y. Choo, C.O. Osuji, P. Gopalan, Rational design of a block copolymer with a high interaction parameter, Macromolecules 47 (2014) 6687–6696.
[21] K. Azuma, J. Sung, Y. Choo, Y. Rokhlenko, J.H. Dwyer, B. Schweitzer, T. Hayakawa, C.O. Osuji, P. Gopalan, Self-assembly of an ultrahigh-chi block copolymer with versatile etch selectivity, Macromolecules 51 (2018) 6460–6467.
[22] T.Y. Lo, A. Dehghan, P. Georgopanos, A. Avgeropoulos, A.C. Shi, R.M. Ho, Orienting block copolymer thin films via entropy, Macromolecules 49 (2016) 624–633.
[23] S. Jang, K. Lee, H.C. Moon, J. Kwak, J. Park, G. Jeon, W.B. Lee, J.K. Kim, Vertical orientation of nanodomains on versatile substrates through self-neutralization induced by star-shaped block copolymers, Adv. Funct. Mater. 25 (2015) 5414–5419.
[24] S. Junnila, N. Houbenov, S. Hanski, H. Iatrou, A. Hirao, N. Hadjichristidis, O. Ikkala, Hierarchical smectic self-assembly of an ABC miktoarm star terpolymer with a helical polypeptide arm, Macromolecules 43 (2010) 9071–9076.
[25] A. Gitsas, G. Floudas, M. Mondeshki, I. Lieberwirth, H.W. Spiess, H. Iatrou, N. Hadjichristidis, A. Hirao, Hierarchical self-assembly and dynamics of a miktoarm star chimera composed of poly(gamma-benzyl-*L*-glutamate), polystyrene, and polyisoprene, Macromolecules 43 (2010) 1874–1881.
[26] T. Isono, I. Otsuka, D. Suemasa, C. Rochas, T. Satoh, R. Borsali, T. Kakuchi, Synthesis, self-assembly, and thermal caramelization of maltoheptaose-conjugated polycaprolactones leading to spherical, cylindrical, and lamellar morphologies, Macromolecules 46 (2013) 8932–8940.
[27] T. Isono, I. Otsuka, Y. Kondo, S. Halila, S. Fort, C. Rochas, T. Satoh, R. Borsali, T. Kakuchi, Sub-10 nm nano-organization in AB(2)- and AB(3)-type miktoarm star copolymers consisting of maltoheptaose and polycaprolactone, Macromolecules 46 (2013) 1461–1469.
[28] H. Kim, B.G. Kang, J.W. Choi, Z.W. Sun, D.M. Yu, J. Mays, T.P. Russell, Morphological behavior of A(2)B block copolymers in thin films, Macromolecules 51 (2018) 1181–1188.
[29] Z.W. Sun, W.X. Zhang, S. Hong, Z.B. Chen, X.H. Liu, S.G. Xiao, E.B. Coughlin, T. P. Russell, Using block copolymer architecture to achieve sub-10 nm periods, Polymer 121 (2017) 297–303.
[30] Z.W. Sun, Z.B. Chen, W.X. Zhang, J. Choi, C.L. Huang, G.J. Jeong, E.B. Coughlin, Y. T. Hsu, X.M. Yang, K.Y. Lee, D.S. Kuo, S.G. Xiao, T.P. Russell, Directed self-assembly of poly(2-vinylpyridine)-*b*-polystyrene-*b*-poly(2-vinylpyridine) triblock copolymer with sub-15 nm spacing line patterns using a nanoimprinted photoresist template, Adv. Mater. 27 (2015) 4364–4370.
[31] H. Kim, M.M.L. Arras, J.P. Mahalik, W.Y. Wang, D.M. Yu, S. Chernyy, M. Goswami, R. Kumar, B.G. Sumpter, K.L. Hong, G.S. Smith, T.P. Russell, Studies on the 3-lamellar morphology of miktoarm terpolymers, Macromolecules 51 (2018) 7491–7499.
[32] V. Grayer, E.E. Dormidontova, G. Hadziioannou, C. Tsitsilianis, A comparative experimental and theoretical study between heteroarm star and diblock copolymers in the microphase separated state, Macromolecules 33 (2000) 6330–6339.
[33] A.J. Convertine, B.S. Sumerlin, D.B. Thomas, A.B. Lowe, C.L. McCormick, Synthesis of block copolymers of 2- and 4-vinylpyridine by RAFT polymerization, Macromolecules 36 (2003) 4679–4681.
[34] T. Arita, M. Buback, P. Vana, Cumyl dithiobenzoate mediated RAFT polymerization of styrene at high temperatures, Macromolecules 38 (2005) 7935–7943.
[35] H.Q. Wu, Y.B. Wan, W.X. Wang, Y. Wang, N.C. Zhou, W. Zhang, X.H. Li, Z. B. Zhang, X.L. Zhu, Hydrogen bonding promoting the controlled radical polymerization of 2-vinyl pyridine: supramonomer for better control, Polym. Chem. 6 (2015) 2620–2625.
[36] C.-F. Huang, A. Yokoyama, T. Yokozawa, Synthesis of polybenzamide-b-polystyrene block copolymer via combination of chain-growth condensation polymerization and atom transfer radical polymerization, J. Polym. Sci., Part A: Polym. Chem. 48 (2010) 2948–2954.
[37] C.-F. Huang, J.-K. Chen, T.-Y. Tsai, Y.-A. Hsieh, K.-Y.A. Lin, Dual-functionalized cellulose nanofibrils prepared through TEMPO-mediated oxidation and surface-initiated ATRP, Polymer 72 (2015) 395–405.
[38] C.-F. Huang, Y. Ohta, A. Yokoyama, T. Yokozawa, Efficient low-temperature atom transfer radical coupling and its application to synthesis of well-defined symmetrical polybenzamides, Macromolecules 44 (2011) 4140–4148.
[39] C.-F. Huang, H.-F. Lee, S.-W. Kuo, H. Xu, F.-C. Chang, Star polymers via atom transfer radical polymerization from adamantane-based cores, Polymer 45 (2004) 2261–2269.
[40] K. Matyjaszewski, D.A. Shipp, J.L. Wang, T. Grimaud, T.E. Patten, Utilizing halide exchange to improve control of atom transfer radical polymerization, Macromolecules 31 (1998) 6836–6840.
[41] B.E. Woodworth, Z. Metzner, K. Matyjaszewski, Copper triflate as a catalyst in atom transfer radical polymerization of styrene and methyl acrylate, Macromolecules 31 (1998) 7999–8004.
[42] N.V. Tsarevsky, W.A. Braunecker, S.J. Brooks, K. Matyjaszewski, Rational selection of initiating/catalytic systems for the copper-mediated atom transfer radical

polymerization of basic monomers in protic media: ATRP of 4-vinylpyridine, Macromolecules 39 (2006) 6817–6824.
[43] K. Min, W. Jakubowski, K. Matyjaszewski, AGET ATRP in the presence of air in miniemulsion and in bulk, Macromol. Rapid Commun. 27 (2006) 594–598.
[44] K.-Y. Lai, Y.-S. Huang, C.-Y. Chu, C.-F. Huang, Synthesis of Poly(*N*-H benzamide)-*b*-poly(lauryl methacrylate)-*b*-poly(*N*-H benzamide) symmetrical triblock copolymers by combinations of CGCP, SARA ATRP, and SA ATRC, Polymer 137 (2018) 385–394.
[45] T. Sarbu, K.Y. Lin, J. Ell, D.J. Siegwart, J. Spanswick, K. Matyjaszewski, Polystyrene with designed molecular weight distribution by atom transfer radical coupling, Macromolecules 37 (2004) 3120–3127.
[46] M.F. Schulz, A.K. Khandpur, F.S. Bates, K. Almdal, K. Mortensen, D.A. Hajduk, S. M. Gruner, Phase behavior of polystyrene-poly(2-vinylpyridine) diblock copolymers, Macromolecules 29 (1996) 2857–2867.